Magnetic and structural correlations in the warwickite Mn$_2$OBO$_3$ Ⓕ

V. Gnezdilov, ⓘD Yu. Pashkevich, ⓘD V. Kurnosov, et al.

COLLECTIONS

Ⓕ   This paper was selected as Featured

View Online   Export Citation   CrossMark

ARTICLES YOU MAY BE INTERESTED IN

Magnetic and structural correlations in the warwickite Mn₂OBO₃

V. Gnezdilov,[1,2,a)] Yu. Pashkevich,[3] V. Kurnosov,[1] O. V. Zhuravlev,[3] D. Wulferding,[2] P. Lemmens,[2]
N. V. Kazak,[4] Yu. V. Knyazev,[4] and S. G. Ovchinnikov[4,5]

AFFILIATIONS

[1] B. Verkin Institute for Low Temperature Physics and Engineering of the National Academy of Sciences of Ukraine, 47 Nauki Ave., Kharkiv 61103, Ukraine
[2] Institute for Condensed Matter Physics, TU Braunschweig, Braunschweig D-38106, Germany
[3] O.O. Galkin Donetsk Institute for Physics and Engineering of the National Academy of Sciences of Ukraine, 46 Nauki Ave., Kyiv 03680, Ukraine
[4] Kirensky Institute of Physics, Federal Research Center KSC SB RAS, Krasnoyarsk 660036, Russia
[5] School of Engineering Physics and Radio Electronics, Siberian Federal University, Krasnoyarsk 660041, Russia

[a)] E-mail: gnezdilov@ilt.kharkov.ua

ABSTRACT

We report a Raman scattering study of single-crystalline homometallic oxyborate Mn₂OBO₃, a compound realizing a one-dimensional ribbon-structure. Phonon excitations as a function of temperature and light polarization are compared to lattice dynamical calculations, giving evidence for a strong coupling between lattice and magnetic degrees of freedom. Furthermore, a broader feature with a distinct structure emerges at low temperatures. Based on our theoretical analysis, we assign this signal to specific two-magnon scattering processes related to high energy flat-band magnon branches.

Published under license by AIP Publishing. https://doi.org/10.1063/1.5121280

1. INTRODUCTION

The interplay of lattice, spin, charge, and orbital degrees of freedom in strongly correlated electron systems yields a large number of interesting phenomena. Particularly, low-dimensional spin systems exhibit rich phase diagrams and unconventional magnetic properties owed to magnetic frustration. The underlying competing interactions are based on the lattice geometry of local moments with antiferromagnetic exchange interactions. The ground state of such systems is characterized by a large degeneracy, preventing the formation of a conventional ordered state down to low temperatures. The interaction of the magnetic system with other degrees of freedom can lift this degeneracy. If the resulting ground state is long range ordered, flat magnon branches may be observed as a fingerprint of the competing interactions.

The large family of warwickites with the chemical formula $M^{2+}M^{3+}OBO_3$ (M^{2+} and M^{3+} are di- and trivalent metals, respectively) has attracted great interest and was studied for more than two decades.[1–16] The crystal lattices of these oxyborate compounds consists of low-dimensional units, namely ribbons of MO_6 edge-sharing octahedra. The presence of transition metal ions in such low-dimensional structures may lead to nontrivial magnetic structures. A big diversity of possible combinations for M^{2+} and M^{3+} positions opens up an opportunity to study intriguing electronic and magnetic properties caused by the interaction between lattice and electronic subsystems.

There are only three homometallic warwickites, Fe_2OBO_3, V_2OBO_3 and Mn_2OBO_3, with M^{2+} and M^{3+} being the same metal ions in different valence states.[17] Fe-warwickite is well studied up to now: it evidences a charge ordering transition around $T_{CO} = 340$ K with an accompanying ortho- rhombic-to-monoclinic structural transition[14] and a magnetic transition around $T_c = 155$ K.[2] At the same time Mn- warwickite has not been studied thoroughly and its physical properties are still under debate.

Initially Mn_2OBO_3 was grown and structurally characterized by R. Norrestam, *et al.*[5] Specific heat and magnetic susceptibility measurements[8] revealed an antiferromagnetic transition at quite high Néel temperature of 104 K and weak ferromagnetic behavior below 70 K.

However, it was later shown that the magnetic transition temperature in Mn_2OBO_3 is significantly lower, with $T_N = 26$ K, and that all other reported features are related to impurity phases.[12] Subsequent thorough experimental studies (electron spin resonance (ESR), magnetization, and thermoelectric power)[11] provided evidence for an intrinsic character of both phase transitions at 105 and 26 K. In view of these results, a revised phase diagram has been proposed. The possibility of a fast electron transfer between the M^{2+} and M^{3+} cations was suggested in the temperature range down to ~105 K, together with an inhomo- geneous (short range) AF ordering of M^{2+} and M^{3+} pairs at temperatures between ~110 K, and finally long range AF order around ~30 K.

Nevertheless the magnetic structure of Mn_2OBO_3 has not been analyzed properly due to the complexity of the crystal structure and many inequivalent superexchange pathways presented in the network.[12] Only very recently a theoretical analysis of the magnetic structure was reported and exchange interactions were estimated.[16] In order to verify the phase diagram and the magnetic structure of Mn homometallic warwickite, we present a Raman spectroscopic study of single crystalline Mn_2OBO_3 covering a wide temperature range from 7 to 295 K. The role of the lattice system in the behavior of magnetic system in Mn_2OBO_3 is one of the focus points of our experimental investigations. Our lattice dynamic calculations support magnetoelastic coupling between lattice and the magnetic subsystems. At low temperatures we observe a structured magnetic excitation which we assign to two-magnon scattering with the contribution of weakly dispersive magnon branches.

2. EXPERIMENT

High-quality single crystals of Mn_2OBO_3 have been grown using the flux technique. Details of the growth of the samples and their characterization are given in Ref. 16.

Raman scattering experiments were performed in quasi-backscattering geometry, using a $\lambda = 532$-nm solid-state laser. The laser power was set to 7 mW with a spot diameter of approximately

100 μm to avoid heating effects. All measurements were carried out in an evacuated closed-cycle cryostat (Oxford/Cryomech Optistat) in the temperature range 7–295 K. The spectra were collected via a triple spectrometer (Dilor-XY-500) by a liquid nitrogen cooled CCD (Horiba Jobin Yvon, Spectrum One CCD-3000 V). Measured specimens were in the form of thin black plates up to 15 mm long and with a cross-sectional area of less than 1.0×0.5 mm. The polarization configuration of the Raman spectra is denoted by $(e_i e_s)$. Laboratory axes X, Y, and Z were chosen to be parallel to the a, b, and c axes of the crystal, respectively.

3. RESULTS AND DISCUSSION

The homometallic warwickites Fe_2OBO_3 and Mn_2OBO_3 have a monoclinic crystal structure at ambient temperature.[3,5] Note that the choice of the axes and their unit cell values differ slightly in the literature (see for example Ref. 12). In our paper, we adopt the choice of the $P2_1/n$ group (#14, Z = 4) with the lattice parameters $a = 9.2919$ Å, $b = 9.5311$ Å, $c = 3.2438$ Å, and $\beta = 90.733°$ according to Ref. 12. The structure of Mn-warwickite, shown in Fig. 1, is described by a herringbone array of infinite ribbons extending along the c axis. The ribbons are constructed from four chains of edge-sharing MnO_6 octahedra. All ribbons are coupled by corner-sharing and trigonal planar BO_3 groups. M^{3+} and M^{2+} ions occupy two inequivalent crystallographic positions, site Mn(1) (within inner chains of ribbons) and site Mn(2) (within outer chains), respectively. The presence of strong Jahn-Teller distortion with an axial elongation of $Mn(1)O_6$ octahedra suggests a charge disproportionation into M^{3+} and M^{2+} ions and $3d_{z^2}$ orbital ordering at the Mn(1) site. Recent high temperature x-ray diffraction experiment has revealed the retention of charge ordering up to high temperatures.[19]

The monoclinic ($P2_1/n$, Z = 4) crystal structure with all atoms at the 4e site symmetry leads to the following 84 vibrational modes: $\Gamma = 21A_g + 21A_u + 21B_g + 21B_u$. Note that only the A_g and B_g modes are Raman-active, leaving 42 expected modes. The corresponding
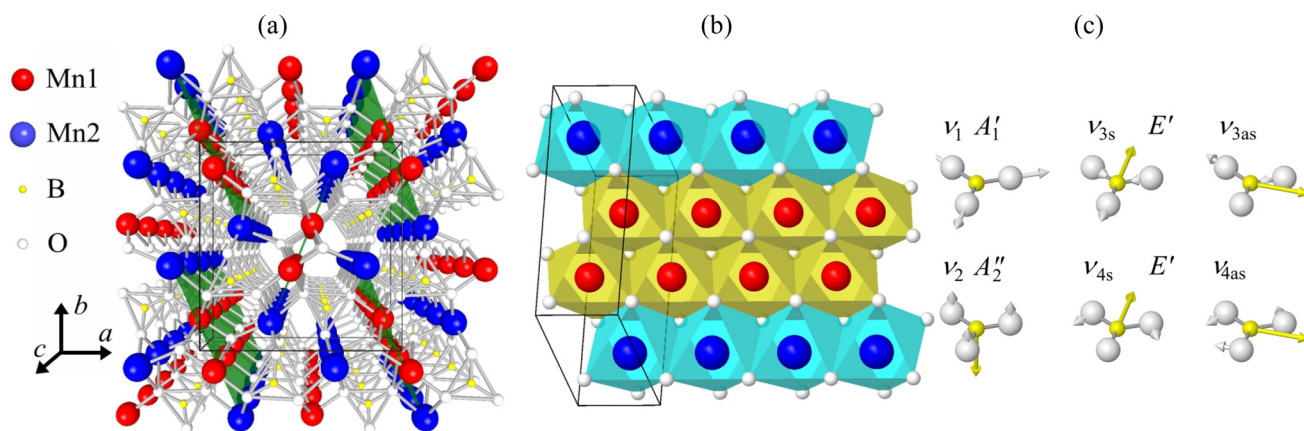

FIG. 1. Extended unit cell image of Mn_2OBO_3. Green colored planes mark the ribbon-like elements (a). Structure of an individual ribbon (b). Intrinsic vibrational modes of the free $[BO_3]^{3-}$ complex (c).

Raman tensors are given by:

$$A_g = \begin{bmatrix} b & 0 & d \\ 0 & c & 0 \\ d & 0 & a \end{bmatrix}, \quad B_g = \begin{bmatrix} 0 & f & 0 \\ f & 0 & e \\ 0 & e & 0 \end{bmatrix}.$$

Figure 2 compares polarized Raman spectra of Mn_2OBO_3 at $T = 295$ and 7 K. The sharpness of the observed phonon modes indicates the high quality of our single crystal. In the frequency region of $25–1500$ cm^{-1}, 34 phonon modes can be identified.

In the phonon spectra of Mn_2OBO_3 the internal BO_3 modes and the external lattice modes which include rotations and translations of the BO_3 unit translations of two metal ions and $O(1)^{2-}$ ion connecting $Mn(1)^{3+}$ inside the ribbons can be separated [Fig. 1(a)]. In addition, all oxygen ions in warwickite form edge-shared octahedra around the transition metal ions [Fig. 1(b)]. The isolated $[BO_3]^{3-}$ anion has a planar structure with D_{3h} symmetry. It is well known that planar XY_3 molecules possess six internal degrees of freedom consisting of two one-dimensional A_1' and A_2'' and two E' two-dimensional irreducible representations (IRP) of the D_{3h} group. Their standard notation ν_1, ν_2, ν_3, and ν_4 [18,19] and characteristic vectors of displacements are presented in Fig. 1(c). We assign phonon modes of the $[BO_3]^{3-}$ unit in accordance with Ref. 19 as follows: 939 cm^{-1} (ν_1, A_1'), 765 cm^{-1} (ν_2, A_2''), 1260 cm^{-1} (ν_3, E'), and 672 cm^{-1} (ν_4, E'). Moreover, only A_1' and E' modes are Raman active, A_2'' and E' modes are active in IR.[18,19]

The octahedral cluster XY_6 with O_h symmetry has 15 vibrational degrees of freedom grouped into six modes ν_1 (A_{1g}), ν_2 (E_g), ν_3 (T_{1u}), ν_4 (T_{1u}), ν_5 (T_{2g}), ν_6 (T_{2u}).[19] Within the framework of the crystal, however, octahedral molecular complexes are bound via common corners, edges or faces. Therefore, a direct assignment of internal XY_6 modes to the crystal vibrational representation is not straightforward.

Overall, the assignment of phonon modes and their symmetry analysis from the experimental spectra is hampered by the low intensity of some lines and a possible leakage from forbidden polarizations. In addition, t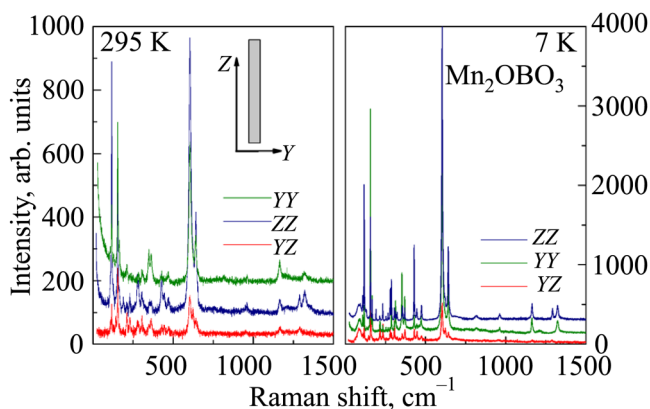he structural BO_3 and MnO_6 units have common ions that are involved in vibrations. In order to assign the symmetries and eigenvectors of the observed optical phonon modes, we compute the Γ-point phonon modes by adopting shell-model lattice dynamical calculations implemented in the General Utility Lattice Program (GULP) package.[20]

The temperature evolution of the spectra measured in ZZ scattering geometry in the frequency region of $25–725$ cm^{-1} is shown in Fig. 3. To get more insight into the phonon dynamics, we analyze the temperature dependence of the phonon line parameters. Phonon lines were fitted with Lorentzian profiles over the whole investigated temperature range and results are presented in Fig. 4 where the temperature dependent parameters of representative phonon modes (154 and 428.7 cm^{-1}) are plotted. With decreasing temperature several distinct features show up. First, upon cooling from room temperature some modes undergo a hardening followed by a saturation in frequency for temperatures around $T^* \approx 100$ K and a softening upon further cooling. Most phonon modes have anomalies at $T_N = 23$ K: a change in the frequency slope or a further hardening towards lower temperatures. Two phonon modes at 108 and 604 cm^{-1} show an unexpected softening with decreasing temperature. In addition, the linewidths of some phonons show an anomalous behavior [see for example Fig. 4(c)] with a substantial deviation between the modelled anharmonicity and the experimental data, and should therefore be regarded as strong evidence for a relaxation mechanism different from multiphonon states. Finally, the integrated intensity of phonons shows a behavior that cannot be described in terms of pure lattice contraction/extension with temperature changing and anharmonicity [see Fig. 4(e) and 4(f)]. Summarizing, our observation of phonon peculiarities at characteristic temperatures T^* and T_N correlates with earlier observations and we consider a coupling of lattice and spin degrees of freedom as the origin for the deviations from anharmonicity in Mn_2OBO_3. This conclusion is underlined by our lattice dynamical calculations, which show that the main

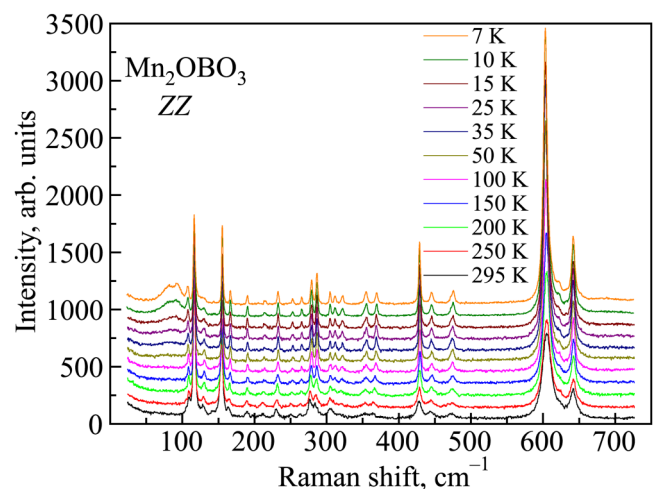**FIG. 2.** Polarized Raman spectra of Mn_2OBO_3 at 295 and 7 K. The inset shows the laboratory axes relatively to the sample shape.

FIG. 3. Temperature dependence of the Raman spectra of Mn_2OBO_3 measured in the ZZ scattering geometry.
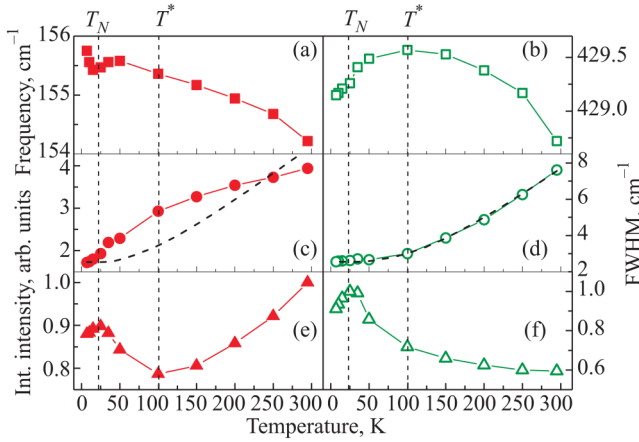
FIG. 4. Temperature dependence of the frequency (a), (b), linewidth (c), (d), and integrated intensity (e), (f) for two phonon lines. Dashed lines in (c), (d) correspond to anharmonic fits using $\Gamma(T) = \Gamma_0[1 + d_j/(\exp(\hbar\omega_0/k_B T)-1)]$[21–23] with d_j being a mode dependent fit parameter.

contribution to the vibration in the region of external lattice modes stems from magnetic ions, which have features near the temperature of magnetic ordering. As an example we present in Table I the normalized eigenvectors for the ions that give the main contribution to the phonon mode at 154 cm^{-1} [see Fig. 4(a), 4(c), and 4(e)].

Figure 5(a) zooms into the low-energy regime. A two-peak structure with maxima around 81 and 92 cm^{-1} is observed at $T = 7$ K. It has larger linewidths than the previously discussed phonon modes. The first band has an asymmetric line shape that can be further decomposed into two bands. This observed structure can be attributed to two-magnon Raman scattering, arising from a double spinflip process involving neighboring sites. In compounds with complex lattice structure, several magnetic ions per unit cell, and competing magnetic exchange interactions the two-magnon Raman spectrum is expected to comprise a few bands.[26] In the case of Mn$_2$OBO$_3$, which can be regarded as a mixed antiferromagnet, one should expect the presence of three bands in the two-magnon spectrum corresponding to the creation of pair excitations on neighboring Mn ions in the combination Mn^{2+}–Mn^{2+}, Mn^{3+}–Mn^{2+} and Mn^{3+}–Mn^{3+}.

With increasing temperatures these excitations merge into a single maximum at ~25 K, undergo a softening and damping, and

TABLE I. The main contributions of ions to the phonon mode at 154 cm^{-1} in the Raman spectra of Mn$_2$OBO$_3$. The normalized eigenvectors are shown for representative ions in 4e Wyckoff positions.

Ion	Normalized eigenvectors		
	x	y	z
Mn1	0.08	−0.04	0.30
Mn2	−1.12	−0.13	−0.12
O4	0.0	0.21	0.0
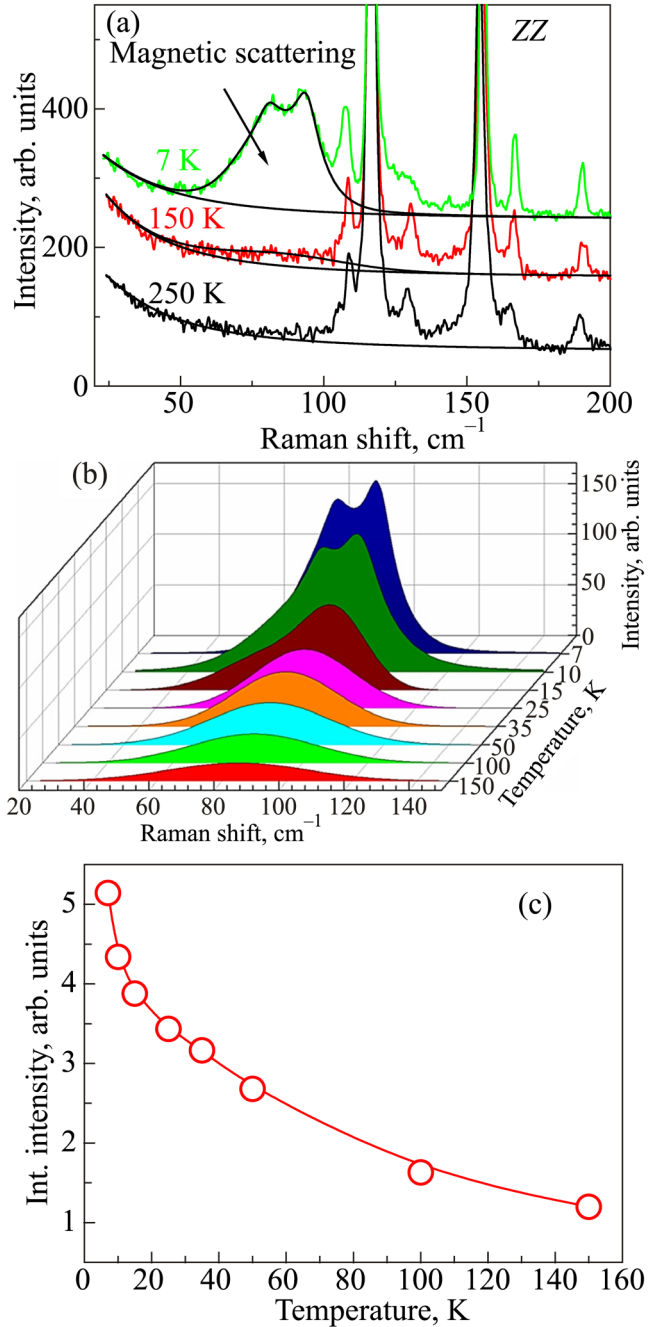
FIG. 5. Temperature dependent low-frequency Raman spectra of Mn$_2$OBO$_3$ (a). Temperature evolution of the two-magnon response in the Raman spectra of Mn$_2$OBO$_3$ (b) and its integrated intensity (c).

then disappear into a diffusive background at temperatures above 150 K. This temperature amounts to T_N [see Fig. 5(b) and 5(c)]. The survival of the zone boundary magnon to exceptionally high temperatures with respect to T_N reflects the fact that in low-

dimensional spin systems magnetic excitations are scaled by an exchange coupling constant J while the classical Neel ordering is caused by interplane or interchain interactions.

Next we turn to the polarization properties of the two-magnon scattering. In our experiment the two-magnon signal was observed with approximately the same intensity both in parallel and crossed scattering configurations. This fact is not surprising and can be attributed to the skewed exchange paths with contributions both parallel and perpendicular to the crystallographic axes.

The antiferromagnetic structure of Mn_2OBO_3 has been identified in the neutron diffraction experiment.[12] The magnetic cell is doubled compared to the crystallographic one in accordance with the observed (1/2 0 1/2) propagation vector of the magnetic structure. In Ref. 12 the $P2_1/n$ space group is assigned to the paramagnetic phase. It was found that magnetic symmetry can be described by the P_c2_1/c (#14.80) Shubnikov group with unitary subgroup $P2_1/c$ and c-antitranslation. The connection between magnetic and structural lattice constants is as follows: $\mathbf{a}_m = -\mathbf{a} + \mathbf{c}$; $\mathbf{b}_m = \mathbf{b}$; $\mathbf{c}_m = \mathbf{a} + \mathbf{c}$. The 16 magnetic ions are distributed within the magnetic cell among four independent $4e$ positions (sublattices) with the initial coordinates: $Mn^{2+}(1)$ (−0.3860, 0.3836, 0.1713); $Mn^{2+}(2)$ (−0.8860, 0.3836, 0.6713); $Mn^{3+}(3)$ (−0.1953, 0.4028, −0.0252); $Mn^{3+}(4)$ (−0.6953, 0.4028, −0.5252).[12] The Mn(1) and Mn(2) positions and Mn(3) and Mn(4) positions are connected to each other by the antitranslation $(\mathbf{a}_m + \mathbf{c}_m)/2$, respectively.

To analyze the magnetic order in Mn_2OBO_3 in detail we introduce linear combinations of the Fourier transformed spins $\mathbf{s}_\alpha^{(i)} = \mathbf{s}_\alpha^{(i)}(\mathbf{k}) = \sum_n \mathbf{s}_{\alpha n}^{(i)} e^{-i\mathbf{k}\mathbf{R}_n}$ of the Mn(i) sublattices. Here $i = 1, 2, 3, 4$ enumerates the $4e$ Wyckoff sites and index α is the number of Mn ion at the respective site (our numbering is sequential to the application of e, 2_y, I, and m_y symmetry operations to the starting coordinates of Mn ions at their respective position).

$$\mathbf{F}^{(i)} = 1/4(\mathbf{s}_1^{(i)} + \mathbf{s}_2^{(i)} + \mathbf{s}_3^{(i)} + \mathbf{s}_4^{(i)});$$
$$\mathbf{L}_1^{(i)} = 1/4(\mathbf{s}_1^{(i)} + \mathbf{s}_2^{(i)} - \mathbf{s}_3^{(i)} - \mathbf{s}_4^{(i)});$$
$$\mathbf{L}_2^{(i)} = 1/4(\mathbf{s}_1^{(i)} - \mathbf{s}_2^{(i)} + \mathbf{s}_3^{(i)} - \mathbf{s}_4^{(i)}); \quad (1)$$
$$\mathbf{L}_3^{(i)} = 1/4(\mathbf{s}_1^{(i)} - \mathbf{s}_2^{(i)} - \mathbf{s}_3^{(i)} + \mathbf{s}_4^{(i)}).$$

The Cartesian components of combinations (1) at $\mathbf{k} = 0$ transform in accordance with irreducible representations (IRP) at the Γ-point of the space group $P2_1/c$ (see Table II).

TABLE II. Magnetic modes or basis functions of the irreducible representations of the unitary subgroup $P2_1/c$ in Mn_2OBO_3. Indices x, y, z indicate the nonzero Cartesian components of the vectors (1) with $\mathbf{y} \parallel \mathbf{b}$ and $\mathbf{z} \parallel \mathbf{c}$. The transformation of permutation modes (1) are presented on the right column.

h	e	2_y	I	m_y	Magnetic modes	Permutation modes
					Mn(i) $i = 1, 2, 3, 4$	
Γ_1	1	1	1	1	$L_{1x}^{(i)}, F_y^{(i)}, L_{1z}^{(i)}$	$\mathbf{F}^{(i)}$
Γ_2	1	−1	1	−1	$F_x^{(i)}, L_{1y}^{(i)}, F_z^{(i)}$	$\mathbf{L}_2^{(i)}$
Γ_3	1	1	−1	−1	$L_{2x}^{(i)}, L_{3y}^{(i)}, L_{2z}^{(i)}$	$\mathbf{L}_1^{(i)}$
Γ_4	1	−1	−1	1	$L_{3x}^{(i)}, L_{2y}^{(i)}, L_{3z}^{(i)}$	$\mathbf{L}_3^{(i)}$

Here $\mathbf{F}^{(i)}$ represents the ferromagnetic moment of the sublattices i and $\mathbf{L}^{(i)}$ are the antiferromagnetic vectors. The magnetic order parameters of a ground state for the known magnetic group must belong to its Γ_1 irreducible representation. Therefore the nonzero magnetic order parameters for each sublattices in Mn_2OBO_3 should be $L_{1x}^{(i)}, F_y^{(i)}, L_{1z}^{(i)}$. The antiferromagnetic state arises due to presence of the antitranslation which provides opposite signs of magnetic order parameters on the $Mn^{2+}(1)$ and $Mn^{2+}(2)$ sublattices and on the $Mn^{3+}(3)$ and $Mn^{3+}(4)$ sublattices.

The type of exchange order (e.g., the type of magnetic order in Heisenberg approximation) can be analyzed by consideration of the permutation symmetry of the magnetic moments. The permutation symmetry accounts for just the mutual orientation of magnetic moments and does not fix its overall direction in space. Respective permutation modes (1) are listed with the corresponding IRP in right column of Table II. In accordance with experimental data of Ref. 12 the main magnetic order parameter in each sublattice is a ferromagnetic moment $\mathbf{F}$ directed along the unique axis $\mathbf{b}$. We will restrict our consideration to Heisenberg nearest neighbor approximation and omit small canting $L_{1x}^{(i)}, L_{1z}^{(i)}$ caused by Dzyaloshinsky-Moriya interactions. Thus, the magnetic ground state of Mn_2OBO_3 can be described as nonzero entities $F_y^{(i)}$ for each sublattice with the conditions $\mathbf{F}^{(1)} \parallel -\mathbf{F}^{(2)} \parallel \mathbf{F}^{(3)} \parallel -\mathbf{F}^{(4)} \parallel \mathbf{b}$-axis and $\mathbf{F}^{(1)} = -\mathbf{F}^{(2)}$ and $\mathbf{F}^{(3)} = -\mathbf{F}^{(4)}$.

We proceed further with a detailed analysis of the exchange topology in Mn_2OBO_3. The main magnetic building blocks in Mn_2OBO_3 are one-dimensional structural units—infinite ribbons running along the $\mathbf{a}_m + \mathbf{c}_m$-direction (see Figs. 1 and 6). A ribbon consists of four chains of edge shared $(MnO)_6$ octahedra. Two chains of Mn^{3+} ($3d^4$ $S = 2$) ions are sandwiched by two chains of Mn^{2+} ($3d^5$ $S = 5/2$) ions which are disposed at the ribbon's edge. The intraribbon exchange interactions feature a triangular topology
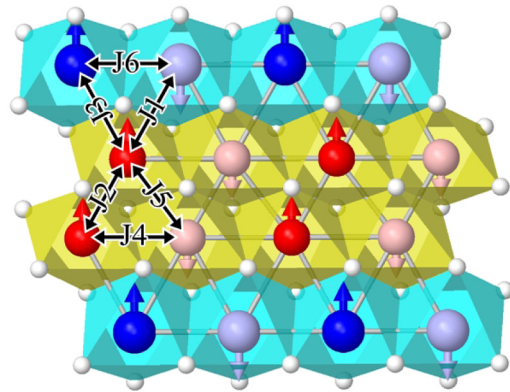

FIG. 6. The crystallographic and magnetic structure of a ribbon in Mn_2OBO_3. The manganese ion positions are shown as $Mn^{3+}(1)$ in red; $Mn^{3+}(2)$ in pink; $Mn^{2+}(3)$ in dark blue; $Mn^{2+}(4)$ in light + blue. The indicated magnetic structure is in accordance with neutron diffraction data[12] with ferromagnetic moments of the sublattices $\mathbf{F}^{(1)} \parallel -\mathbf{F}^{(2)} \parallel \mathbf{F}^{(3)} \parallel -\mathbf{F}^{(4)} \parallel \mathbf{b}$-axis. The experimentally observed canting of the magnetic moments in Mn(3) and Mn(4) sublattices are omitted. The enumeration of exchange interaction is the same as in Ref. 16.

of the Mn ions mutual arrangement, resulting in a highly frustrated magnetic ground state. A small variation of the Mn-Mn distances in the triangles partially removes this frustration. However, the model estimation of the intraribbon exchange interactions[16] reveals all of them to be antiferromagnetic. The Mn−O−Mn bonding angles between $Mn^{3+}(1, 2)$ and $Mn^{2+}(3, 4)$ sublattices also bring in some degree of uncertainty about the estimated exchange values. A close inspection of these angles shows that in respective edge shared $(Mn^{3+}O_6)−(Mn^{2+}O_6)$ octahedra one of the Mn−O−Mn bond angles is smaller than 95°, while another one is larger. A strong deviation of bond angles around a critical average value, at which the exchange interaction can change the sign, is the main source of uncertainty. In general six exchange integrals are sufficient to describe intraribbon magnetic order (see Fig. 6). We adopt the same enumeration of exchange integrals as in Ref. 16 by assigning them in accordance to the Mn−Mn distances.

Structurally, Mn_2OBO_3 consists of two ribbons that are inclined to each other (see Fig. 1). The interribbon nearest-neighbor exchange interactions are realized through interactions between Mn(3,4) and Mn(1,2) sublattices. Here, every Mn^{2+} ion at the ribbon edge interacts with triangles of Mn^{3+} ions from the neighboring ribbon via the only Mn−O−Mn pathway that is involved in building corner-shared octahedra. This topology is also a source of frustration, as Mn^{3+} triangles include either two ions from $Mn^{3+}(1)$ and one ion from $Mn^{3+}(2)$ sublattices or vice versa. However, the interribbon Mn−Mn distances do exceed 3.5 Å and in model calculations[16] three antiferromagnetic interribbon exchange interactions are weaker than intraribbon ones. One can conclude that magnetic ordering in Mn_2OBO_3 can be described in a minimal model with nine nearest-neighbor exchange interactions. Notice the absence of the intra sublattice exchange interactions as a special structural feature of Mn_2OBO_3.

Sixteen magnetic ions define the spin dynamics of Mn_2OBO_3 with sixteen spin wave branches. Within the Heisenberg approximation and a collinear antiferromagnetic structure two out of sixteen magnon branches must be gapless Goldstone modes. The highest intensity of a two-magnon scattering process forms from the spectral region of spin waves with a high density of states. Such a region is usually found at the boundary of the Brillouin zone. However, in the case of dispersionless spin-waves, so called flat-band modes, the contribution can be detected all throughout the Brillouin zone, even from the Γ-point.[27]

To elucidate the origin of the two-magnon signal in Mn_2OBO_3 we perform a calculation of the spin-wave spectrum in Heisenberg nearest-neighbor approximation using the above described magnetic structure adopted from Ref. 12. The calculations have been done in linear spin-wave approximation with the help of the SpinW code.[28] As a starting point we choose the values of exchange integrals obtained by model estimation in Ref. 16. Our calculations find that the high frustration caused by the same antiferromagnetic sign of this set of exchange integrals (here we use notation $J_{AF} > 0$) leads to a ground state instability. The strongest impact comes from the frustration along $Mn^{2+}(1)−Mn^{3+}(3)$ ferromagnetic bonding, whereas $J3 > 0$ is antiferromagnetic. We assume that the reason for the wrong estimation of the J3 exchange is the large variation in Mn−O−Mn bond angles. The ground state stability can be restored once J3 becomes ferromagnetic. In the following calculations

we use the exchange integrals: $J1 = 3.58$ K, $J2 = 1.28$ K, $J3 = −6.07$ K, $J4 = J5 = 4.47$ K, $J6 = 4.63$ K, $J7 = −2.14$ K, $J8 = 0.42$ K, and $J9 = 0.58$ K. Except for the sign of J3 and J7, the absolute values of this set of exchange integrals are slightly smaller than those reported in Ref. 16. The corresponding calculated spin-wave dispersions of Mn_2OBO_3 are shown in Fig. 7.

The most striking feature of the calculated spin-wave spectrum is the small dispersion of the high energy (flat-band) spin-waves. At the Γ-point eight doubly degenerate spin-waves appear at 40.2, 40.56, 46.46, and 47.72 cm^{-1}.

Their absolute energies as well as their energy difference correlates well with the double peak feature seen at 81.4 and 91.6 cm^{-1} in the two-magnon spectrum shown in parallel polarization in Fig. 5. Furthermore, the different symmetry of these branches allows combining them to contribute to cross-polarized two-magnon scattering as observed in our experiment. The appearance of flat-band modes can be connected with the specific quasi-onedimensional ribbon chain topology of the Mn_2OBO_3 crystal structure. Recently, flat-band spin dynamics have been uncovered in the saw-tooth spin chain compound $Fe_2O(SeO_3)_2$.[25]

In summary, we have measured polarized Raman scattering spectra of single-crystalline homometallic oxyborate Mn_2OBO_3 in the temperature range of 7–295 K. This compound is a realization of a one-dimensional ribbon structure along the c-axis. Long-range magnetic order is established below $T_N = 23$ K and yields pronounced phonon anomalies. Besides anomalies in optical phonons, we have observed excitations of high intensity related to the long-range magnetic order. We assign them to two-magnon signals, connected to the specific form of the one-magnon spectrum of the magnetic ribbon lattice with a set of dispersionless spin-wave branches. The
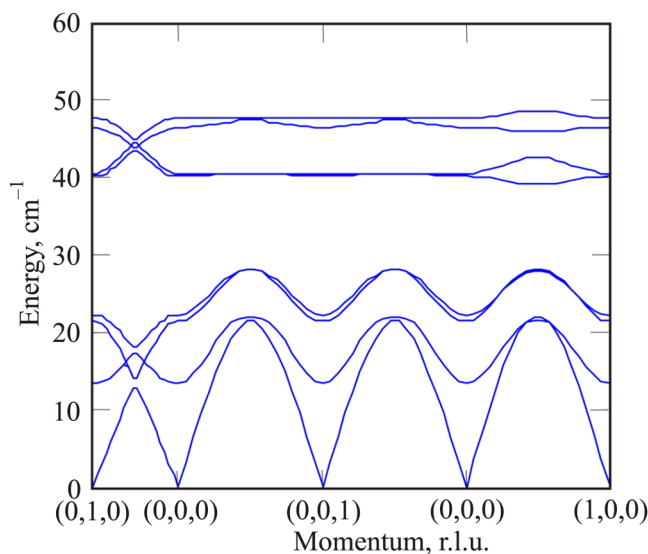

FIG. 7. Spin-wave dispersions in Mn_2OBO_3 along high symmetry lines calculated in the nearest-neighbor Heisenberg approximation. All spin branches are doubly degenerate due to the presence of an antitranslation symmetry element in the Shubnikov group.

minimal set of exchange coupling constants has been estimated based on Raman data and results of linear spin-wave calculations.

REFERENCES

[1] J. P. Attfield, J. F. Clarke, and D. A. Perkins, Physica B **180**, 581 (1992).

[2] J. P. Attfield, A. M. T. Bell, L. M. Rodriguez-Martinez, J. M. Greneche, R. J. Cernik, J. F. Clarkez, and D. A. Perkins, Nature (London) **396**, 655 (1998).

[3] J. P. Attfield, A. M. T. Bell, and D. A. Perkins, J. Mater. Chem. **9**, 205 (1999).

[4] J. C. Fernandes, R. B. Guimarães, M. A. Continentino, H. A. Borges, J. V. Valarelli, and A. Lacerda, Phys. Rev. B **50**(16), 754 (1994).

[5] R. Norrestam, M. Kritikos, and A. Sjödin, J. Solid State Chem. **114**, 311 (1995).

[6] R. B. Guimarães, J. C. Fernandes, M. A. Continentino, H. A. Borges, C. S. Moura, J. B. M. da Cunha, and C. A. dos Santos, Phys. Rev. B **56**, 292 (1997).

[7] M. A. Continentino, B. Boechat, R. B. Guimarães, J. C. Fernandes, and L. Ghivelder, J. Magn. Magn. Mater. **226**, 427 (2001).

[8] M. A. Continentino, A. M. Pedreira, R. B. Guimarães, M. Mir, J. C. Fernandes, R. S. Freitas, and L. Ghivelder, Phys. Rev. B **64**, 014406 (2001).

[9] A. P. Douvalis, V. Papaefthymiou, and G. Kallias, J. Phys. Condens. Matter **12**, 177 (2000).

[10] A. P. Douvalis, V. Papaefthymiou, and T. Bakas, Hyperfine Interact. **126**, 319 (2000).

[11] B. Rivas-Murias, F. Rivadulla, M. Sánchez-Andújar, A. Castro-Couceiro, M. A. Señarís-Rodríguez, and J. Rivas, Chem. Mater. **18**, 4547 (2006).

[12] R. J. Goff, A. J. Williams, and J. P. Attfield, Phys. Rev. B **70**, 014426 (2004).

[13] M. Matos and R. B. Oliveira, Int. J. Quantum Chem. **106**, 2737 (2006).

[14] M. Angst, R. P. Hermann, W. Schweika, J. W. Kim, P. Khalifah, H. J. Xiang, M. H. Whangbo, D. H. Kim, B. C. Sales, and D. Mandrus, Phys. Rev. Lett. **99**, 256402 (2007).

[15] S. Li, J. Leng, Y. Fan, C. Fu, H. Shen, Y. Xue, and D. Xu, Phys. Status Solidi A **208**, 114 (2011).

[16] N. V. Kazak, M. S. Platunov, Y. V. Knyazev, N. B. Ivanova, O. A. Bayukov, A. D. Vasiliev, L. N. Bezmaternykh, V. I. Nizhankovskii, S. Y. Gavrilkin, K. V. Lamonova, and S. G. Ovchinnikov, J. Magn. Magn. Mater. **393**, 316 (2015).

[17] E. M. Carnicom, K. Górnicka, T. Klimczuk, and R. J. Cav, J. Solid State Chem. **265**, 319 (2018).

[18] https://materialsproject.org/materials/mp-32009/.

[19] N. V. Kazak, M. S. Platunov, Y. V. Knyazev, E. M. Moshkina, L. A. Solovyov, S. N. Vereshchagin, Y. L. Mikhlin, A. A. Veligzhanin, A. L. Trigub, and S. G. Ovchinnikov, Physica B Condens. Matter **560**, 228 (2019).

[20] M. M. Sushchinskii, *Raman Spectra of Molecules and Crystals* (John Wiley & Sons, 1972).

[21] K. Nakamoto, "Infrared and Raman spectra of inorganic and coordination compounds, theory and applications," in *Inorganic Chemistry* (John Wiley & Sons, Hoboken, 2008).

[22] G. D. Gale, ""GULP: A computer program for the symmetry- adapted simulations of solids," J. chem. Soc., Faraday Trans. **93**, 629 (1997).

[23] P. G. Klemens, Phys. Rev. **148**, 845 (1966).

[24] M. Balkanski, R. F. Wallis, and E. Haro, Phys. Rev. B **28**, 1928 (1983).

[25] K. Wakamura and T. Arai, J. Appl. Phys. **63**, 5824 (1988).

[26] M. G. Cottam and D. J. Lockwood, *Light Scattering in Magnetic Solids* (Wiley, New York, 1985).

[27] V. P. Gnezdilov, Y. G. Pashkevich, V. S. Kurnosov, O. V. Zhuravlev, D. Wulferding, P. Lemmens, D. Menzel, E. S. Kozlyakova, A. Y. Akhrorov, E. S. Kuznetsova, P. S. Berdonosov, V. A. Dolgikh, O. S. Volkova, and A. N. Vasiliev, Phys. Rev. B **99**, 064413 (2019).

[28] S. Toth and B. Lake, J. Phys. Condens. Matter **27**, 166002 (2015).

Translated by AIP Author Services